Supporting Information

S-vacancy-assisted fast charge transport and oriented ReS_2 growth in twin crystal $Zn_xCd_{1-x}S$: atomic-level heterostructure for dual-functional photocatalytic conversion

Guiyang Yu,[a,*] Ke Gong,[b,*] Xiang Li,[a] Luyan Guo,[b] Xiyou Li,[b] Debao Wang[a,*]

[a] Key Laboratory of Optic-electric Sensing and Analytical Chemistry for Life Science (MOE), College of Chemistry and Molecular Engineering, Qingdao University of Science and Technology, Qingdao, 266042, PR China.

[b] School of Materials Science and Engineering, China University of Petroleum (East China), Qingdao, 266580, China.

Correponding Email:

yugy3413@qust.edu.cn; dbwang@qust.edu.cn; gongkeupc@gmail.com

Contents

Fig. S12 Density of states (DOS) of ZCS and *Sv*-ZCS.

Fig. S13 Mott-Schottky plots of (a) ZCS, (b) *Sv*-ZCS and (c) ReS_2 samples. (d) Schematic diagram of band structure for as-prepared photocatalysts.

Fig. S14 UV-Vis diffuse reflectance spectra of ReS_2/*Sv*-ZCS with different content of ReS_2.

Fig. S15 The peak areas for the known product concentrations were used to generate a calibration curve of (a) benzyl alcohol, (c) benzaldehyde and (e) H_2. High performance liquid chromatography (HPLC) analysis chromatogram of (b) benzyl alcohol and (d) benzaldehyde.

Fig. S16 (a) H_2 and (b) benzaldehyde production amount with different reaction time upon ZCS, *Sv*-ZCS, ReS_2/ZCS and ReS_2/*Sv*-ZCS samples.

Fig. S17 (a) HPLC analysis of intermediate products and (b) GC analysis of H_2 products over ZCS sample in the photocatalytic reaction process.

Fig. S18 (a) HPLC analysis of intermediate products and (b) GC analysis of H_2 products over *Sv*-ZCS sample in the photocatalytic reaction process.

Fig. S19 (a) HPLC analysis of intermediate products and (b) GC analysis of H_2 products over ReS_2/*Sv*-ZCS sample in the photocatalytic reaction process.

Fig. S20 (a) HPLC analysis of intermediate products and (b) GC analysis of H_2 products over ReS_2/ZCS sample in the photocatalytic reaction process.

Fig. S21 Photocatalytic activity of (a) H_2 and (b) benzaldehyde production amount, (c) benzyl-alcohol conversion with different reaction time upon ZCS and ReS_2/*Sv*-ZCS samples with different amount of ReS_2.

Fig. S22 (a and b) TEM and (c-e) HRTEM images of the ReS_2/*Sv*-ZCS sample after reaction.

Fig. S23 (a) XRD patterns, (b) Cd 3d, (c) Zn 2p, and (d) Re 4f XPS spectra of fresh and used ReS_2/*Sv*-ZCS samples.

Fig. S24 Photocatalytic activity of (a) H_2 and (b) benzaldehyde evolution amount, (c) benzyl alcohol conversion with different solvent condition upon 10% ReS_2/*Sv*-ZCS sample.

Fig. S25 Photocatalytic activity of (a) H_2 and (b) benzaldehyde evolution amount, (c)

Experimental Section

1. Material Characterization

The crystallite property was examined using the X-ray diffraction (XRD) characterization containing a Rigaku X-ray diffractometer of Cu Kα radiation (λ=1.5418 Å, 50 kV, 200 mA). The scanning rate is 10 º/min from 10º to 70º. The morphology and holey property were investigated using JEOL JSM-6700F field-emission scanning electronic microscope (SEM) and JEM 2100 transmission electron microscopy (TEM) with the accelerating voltage of 10 kV and 200 kV, respectively. Fourier transform infrared spectra (FTIR) was performed to determine the change of functional moieties with Bruker V70 spectrometer. Hitachi UV-3900 spectrophotometer was used to analyse the UV-vis diffused reflectance spectra (DRS) of the samples, in which $BaSO_4$ acts as blank reference. The surface areas and pore distribution were determined by N_2 adsorption/desorption isotherms and Brunauer-Emmett-Teller (BET) method. The sample was heated to 150 ºC maintaining 5 h in order to evacuate any moisture and solvent molecules inner the pore. The element composition and chemical property were examined by X-ray photoelectron spectroscopy (XPS). The excitation source was Thermo Escalab 250 Xi Mg Kα of 1254.6 eV and the calibrated process was used C 1s peak at 284.6 eV as standard. The contact potential difference between the samples and the spectrometer, versus normal hydrogen electrode (NHE) at pH = 7, was estimated using the formula $E_{NHE} / V = \Phi + VB_{max} - 4.44$ (E_{NHE}: potential of normal hydrogen electrode; Φ of 3.88 eV: the electron work function of the spectrometer). Steady-state photoluminescence (PL) and time

resolved fluorescence spectra were performed on FLS980 (Edinburgh instrument Ltd, England) at room temperature. The electronic nature and paramagnetic species of samples were measured on a JES-FA200 EPR spectra. The sweeping magnetic field was at room temperature and experimental parameters were microwave frequency at uF9441.704, microwave power 20 mW, modulation frequency 100 kHz, and attenuator 10 dB, respectively. For in-situ EPR measurements, 10% ReS_2/*Sv*-ZCS powder was dispersed in a mixed solution of benzyl alcohol containing DMPO (4 mM), which was used as a spin-trapping agent, by ultrasonic treatment. Afterwards, the suspension was injected into a glass capillary and the glass capillary was placed in a sealed glass tube under N_2 atmosphere. The sealed glass tube was placed in the microwave cavity of EPR spectrometer and was irradiated with Xe lamp ($\lambda \geq 420$ nm) during EPR measurements at room temperature.

2. Photoelectrochemical measurements

The transient photocurrent responses, and electrochemical impedance spectroscopy (EIS) were investigated on a CHI760D electrochemical workstation (Shanghai Chenhua Instrument Corp., China) in a conventional three-electrode system composed of a Pt sheet counter electrode, a saturated Ag/AgCl as reference electrode and a working electrode. Firstly, the working electrode was fabricated by spin-coating ethanol suspensions onto pre-cleaned FTO glass (1×1 cm^{-2}) surface. Typically, 5 mg sample was dispersed evenly in 2 mL ethanol with 10 μL Nafion solution, followed by ultrasonic treatment for 1 h to form homogeneous solution. The above solution was dipped (40 μL) and spin-coated (200 $r \cdot min^{-1}$, 10 s) onto the pre-cleaned FTO conductive

glass surface, and then dried at room temperature. The above coating process was repeated ten times. Moreover, 0.5 M Na_2SO_4 aqueous solution was used as supporting electrolyte. A 300 W Xe lamp equipped with a 420 nm optical cutoff filter was used at light source. The photo-responsive signals were measured by I-t curves and the electrochemical impedance spectroscopy was tested at a frequency range from 10^5 to 0.01 Hz.

3. Density-functional-theory (DFT) calculations

All calculations are performed with the Vienna Ab-initio Simulation Package (VASP) in the framework of density functional theory (DFT).[1,2] The projector augmented wave (PAW) method [3,4] is used to describe the electrons-ionic interactions and the generalized gradient approximation (GGA) together with the Perdew-Burke-Ernzerhof (PBE)[5] is employed to describe all exchange and correlation effects. Grimmes's dispersion correction D3 is used to account for the vdW interaction.[6,7] A cutoff energy of 400 eV is used to ensure the precision of calculations. Convergence criteria are set to be 10-5 eV for energy and 0.03 eV/Å for the forces. Brillouin zone is sampled using the Monkhorst–Pack by a 6 × 6 × 1 k-point grid. $Zn_xCd_{1-x}S$ is a semiconductor, Gaussian smearing with a width of 50 meV was used for the occupation of electronic levels. To simulate the ReS_2/*Sv*-ZCS composites, ReS_2 were put on a (2 × 2) stoichiometric *Sv*-ZCS surface slab. To get the exact DOS results, we increased the number of k-point and use 9 × 9 × 1 k-point grid.

4. Photocatalytic Reaction Experiment

Photocatalytic selective oxidation of benzyl alcohol with intergated H_2 evolution

was carried out in a double-walled quartz reactor with the top-irradiation. The temperature of the solution was maintained at 298 K by a flow of circulating water. In detail, 10 mg photocatalyst was added into 10 mL of deionized water containing 0.5 mmol of benzyl alcohol. The reaction suspension was bubbled with high purity nitrogen for 30 min to remove the air. Then 300 W Xenon lamp ((Beijing Perfectlight Technology Co., Ltd., Microsolar 300) equipped with 420 nm cut-off filter was used to provide the visible light irradiation. The efficient irradiated area was about 16.5 cm^2 and the light intensity is controlled to be 100 $mW \cdot cm^{-2}$. The amount of evolved H_2 gas was determined by gas chromatography (GC 7900) equipped with a thermal conductivity detector and a 4 m 5 Å molecular sieve columns. The liquid products were filtered through a 0.22 μm Nylon syringe filter, and then analyzed by high-performance liquid chromatography (HPLC, Shimadzu LC-20 A, column oven CTO-20 A, pump LC-20 A, UV detector SPD-20 A, autosampler). The column for HPLC measurement was a Shim-pack GIST C18 (250×4.6 mm I.D., 5 μm). The column oven was kept at 35 ºC. The injected sample (either 1 μL in volume) was eluted with acetonitrile-water (6:4) aqueous solution at a fixed flow rate (1 mL/min). The UV detector was set at 210 nm so that the absorption due to reactants and products can be easily detected.

The apparent quantum efficiency was measured under the same photocatalytic reaction except for the wavelength of irradiation light. The apparent quantum efficiency of different amounts of photocatalysts in one continuous reaction under visible light with different wavelengths of 420, 450, 500, 550, 600 nm were measured. Apparent quantum efficiency at different wavelengths was calculated by the following function.

The band-pass and cutoff filters and a photodiode were used in measurement.

$$\text{AQE}\ (\%) = \frac{\text{Number of reacted electrons}}{\text{Total number of incident photons}} \times 100$$

$$= \frac{2 \times \text{The number of evoluted } H_2 \text{ molecules}}{\text{Total number of incident photons}} \times 100$$

Note 1. The role of the introduction of NaOH is controlling crystallization rate of hexagonal phase and cubic phase in forming twin crystal phase.

The NaOH-assisted hydrothermal method is firstly reported in the literature of Liejin Guo's group for preparing $Cd_{1-x}Zn_xS$ solid solution with nano-twin structure.[8] In this literature, Liejin Guo and his co-workers found that adding NaOH aqueous solution (4 $mol \cdot L^{-1}$) is the key factor for forming nano-twin $Cd_{1-x}Zn_xS$ with hexagonal and cubic phase. The absence of NaOH results in the $Cd_{1-x}Zn_xS$ solid solution with single phase. Adding NaOH could firstly react with Zn^{2+} and Cd^{2+} to form the mixture of $Cd(OH)_2$ and $Zn(OH)_2$. Then the replacement reaction occurs between sulfur source (thioacetamide) and the mixture of $Cd(OH)_2$ and $Zn(OH)_2$ during hydrothermal condition. The rate of replacement reaction is thermodynamically driven, which could control crystallization rate.

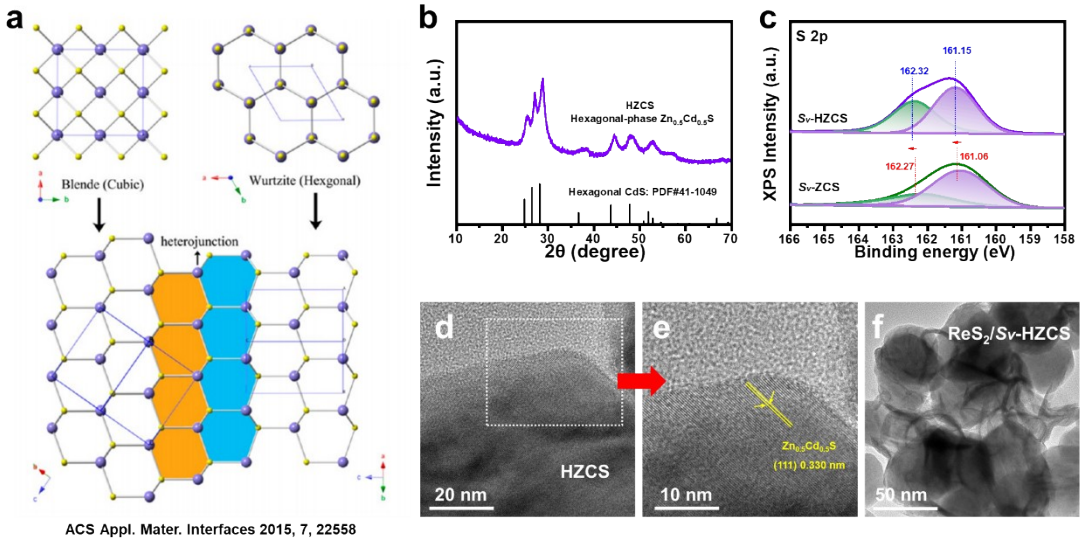

Fig. S1 (a) Schematic representation of crystal structure of cubic and hexgonal phases for $Zn_{1-x}Cd_xS$ solid solution according to the reference ACS Appl. Mater. Interfaces 2015, 7, 22558. (b) XRD pattern of HZCS sample. (c) S 2p XPS spectra of *Sv*-ZCS and *Sv*-HZCS samples. HRETM images of (d and e) HZCS and (f) ReS_2/*Sv*-HZCS samples.

Note 2. The effect of hexagonal and cubic phase-segments on the creation of S-vacancies via H_2 reduction and the deposition of the ReS_2 co-catalyst.

In the structure of $Zn_{0.5}Cd_{0.5}S$ solid solution, the existence of hexagonal and cubic phases could form heterojunction. Hao Ming Chen's group has simulated the structural model of cubic and hexagonal phases for $Zn_{1-x}Cd_xS$ (Fig. S1a). It shows that the Zn/Cd atoms connected to four S atoms to construct tetrahedral subunit ([Zn/Cd]S_4) and this subunit further connect each other via sharing the corners to build the three-dimensional structures. Compared with single-phase $Zn_{0.5}Cd_{0.5}S$, the connected boundary of heterojunction in twin-crystal $Zn_{0.5}Cd_{0.5}S$ possesses distorted spatial structure (different arrow direction between hexagonal and cubic crystal in Fig. S1a). It is well known that the chemical bond of distorted structure is weakened and is more likely to be activated.

When the $Zn_{0.5}Cd_{0.5}S$ is treated in H_2 atmosphere under 150 ºC, the Metal-S (Zn-S or Cd-S) bond in boundary of two phases is easier to be broken. The S atom leaves from the lattice position and forms H_2S gas with H_2. Therefore, it is reasonable to speculate that the presence of hexagonal and cubic phase-segments in $Zn_{0.5}Cd_{0.5}S$ facilitates the formation of S-vacancies via H_2 reduction.

Furthermore, additional experiments and characterizations are supplemented to verify above speculation. The single hexagonal-phase $Zn_{0.5}Cd_{0.5}S$ solid solution was prepared via the common hydrothermal method,[9] which is denoted as HZCS. XRD pattern (Fig. S1b) and TEM image (Fig. S1d and S1e) show the presence of hexagonal crystal without any phase structure. Using the same reduced-treatment condition (H_2 atmosphere under 150 ºC) as twin-crystal *Sv*-$Zn_{0.5}Cd_{0.5}S$, *Sv*-HZCS sample was obtained and the ReS_2 (10 wt%) was deposited on the surface of *Sv*-HZCS to get ReS_2/*Sv*-HZCS sample. Compared with *Sv*-ZCS, ICP analysis shows that the content of S element for *Sv*-HZCS is higher (Table S1), which indicates that the number of lost S atom from HZCS is less than twin-crystal ZCS. S 2p XPS spectra of twin-crystal *Sv*-ZCS (Fig. S1c) shows obvious high-shifted binding energy than that of *Sv*-HZCS, which further demonstrates more S vacancies are presence in twin-crystal ZCS.[10]

When the S vacancy is formed on the surface of $Zn_{0.5}Cd_{0.5}S$ solid solution, S vacancy region could provide the deposition site for ReO_4^- from spatial scale and facilitate the uniform growth of ReS_2 particle. As shown in Fig. S1f, the TEM image of ReS_2/*Sv*-HZCS show several aggregated particles for ReS_2 crystalline phase.

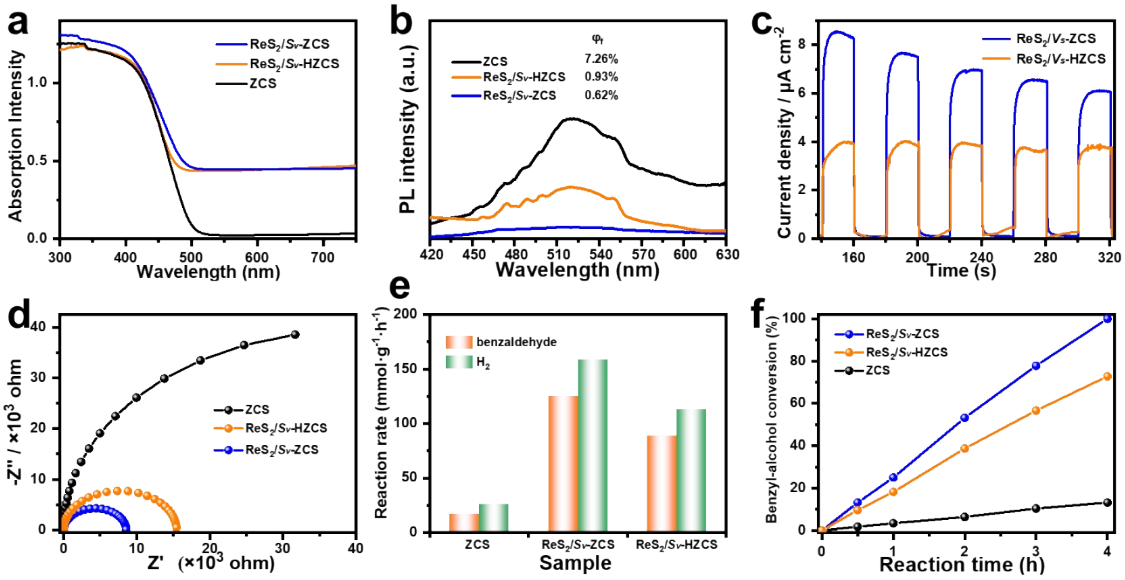

Fig. S2 (a) UV-Vis diffuse reflectance spectra, (b) PL spectra, (c) Photocurrent plots and (d) Nyquist plots of ZCS, ReS_2/*Sv*-HZCS and ReS_2/*Sv*-ZCS samples. Photocatalytic activity of (e) the reaction rate including benzaldehyde and H_2 products and (f) benzyl-alcohol conversion with time course upon ZCS, ReS_2/*Sv*-HZCS and ReS_2/*Sv*-ZCS samples.

Note 3. UV-vis spectra in Fig. S2a shows that both ReS_2/*Sv*-ZCS and ReS_2/*Sv*-HZCS possess strong visible-absorption intensity from ReS_2, while ReS_2/*Sv*-ZCS is observed more clear Urbach tail than ReS_2/*Sv*-HZCS due to more contribution from S vacancy (discussed above). Compared with ReS_2/*Sv*-HZCS, ReS_2/*Sv*-ZCS exhibits obvious quenched PL intensity and lower absolute fluorescence quantum yield (0.62% *vs.* 0.93%). This result demonstrates that the recombination of photoexcited carriers in ReS_2/*Sv*-ZCS is lower and twin-crystal is beneficial for the charge separation. In addition, Fig. S2c shows that the photocurrent intensity for ReS_2/*Sv*-ZCS is more enhanced than that of ReS_2/*Sv*-HZCS. The EIS Nyquist plots (Fig. S2d) presents the arc radius of ReS_2/*Sv*-ZCS is smaller than that of ReS_2/*Sv*-HZCS. These

electrochemical results further indicate the improved charge separation and transfer upon twin-crystal nature. Using the same reaction condition, photocatalytic redox coupling reaction rate upon ReS_2/*Sv*-HZCS and ReS_2/*Sv*-ZCS samples is compared. As shown in Fig. S2e, ReS_2/*Sv*-ZCS exhibits the photocatalytic H_2 and benzaldehyde evolution rate with 159 $mmol \cdot g^{-1} \cdot h^{-1}$and 125 $mmol \cdot g^{-1} \cdot h^{-1}$, respectively, which is higher than that upon ReS_2/*Sv*-HZCS sample (89 $mmol \cdot g^{-1} \cdot h^{-1}$ (benzaldehyde) and 113 $mmol \cdot g^{-1} \cdot h^{-1}$ (H_2)). Based on the above analysis, it is concluded that the twin-crystal structure in ReS_2/*Sv*-ZCS promotes the formation of S vacancy, enhances the light-absorption, improves the charge separation and transfer, and contributes to the excellent photocatalytic redox coupling reaction efficiency for H_2 evolution and benzyl alcohol oxidation.

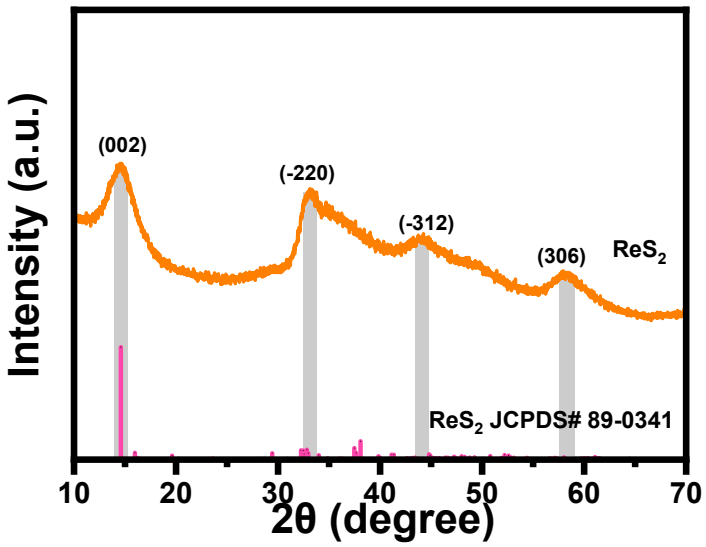

Fig. S3 XRD patterns of ReS_2 and corresponding standard JCPDS.

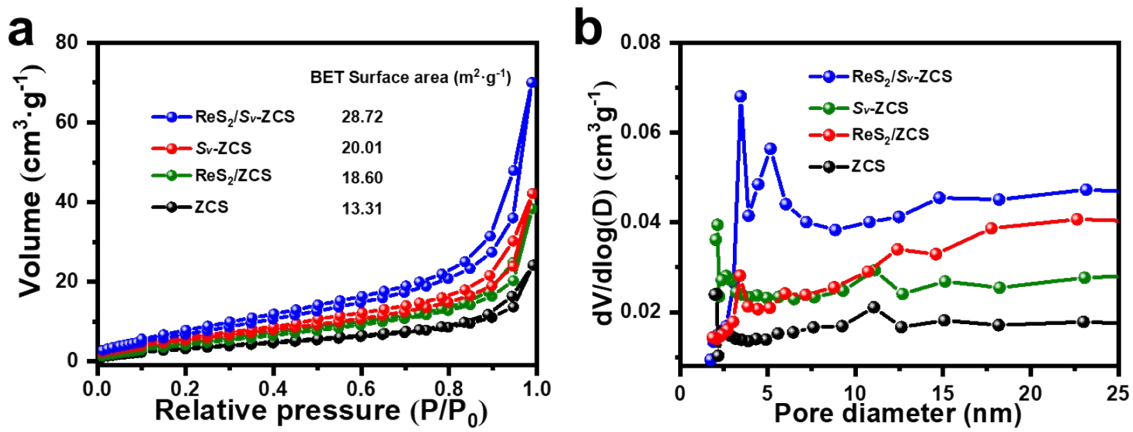

Fig. S4 (a) Nitrogen adsorption-desorption isotherms (inset is the BET surface area), (b) pore size distribution of ZCS, *Sv*-ZCS, ReS_2/ZCS and ReS_2/*Sv*-ZCS samples.

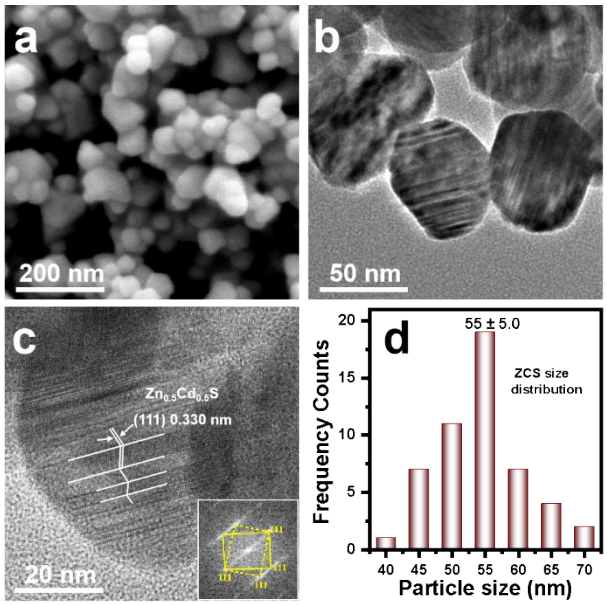

Fig. S5 (a) SEM image, (b) TEM image, (c) HRTEM image and (d) particle size distribution of ZCS sample.

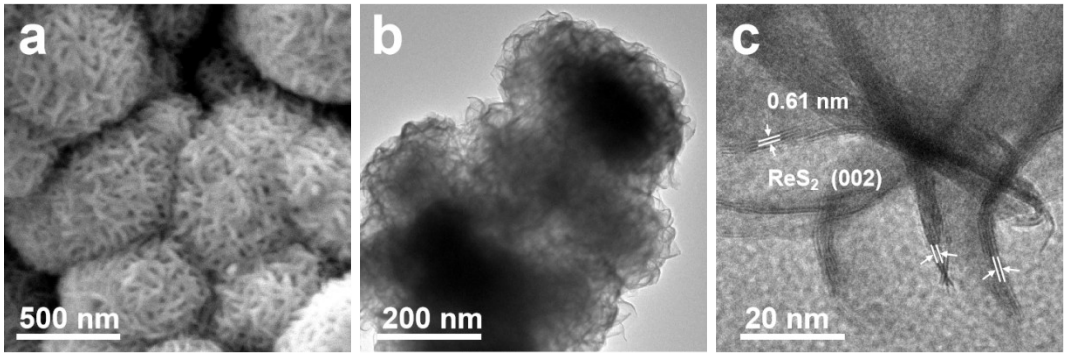

Fig. S6 (a) SEM image, (b) TEM image, (c) HRTEM image of ReS_2.

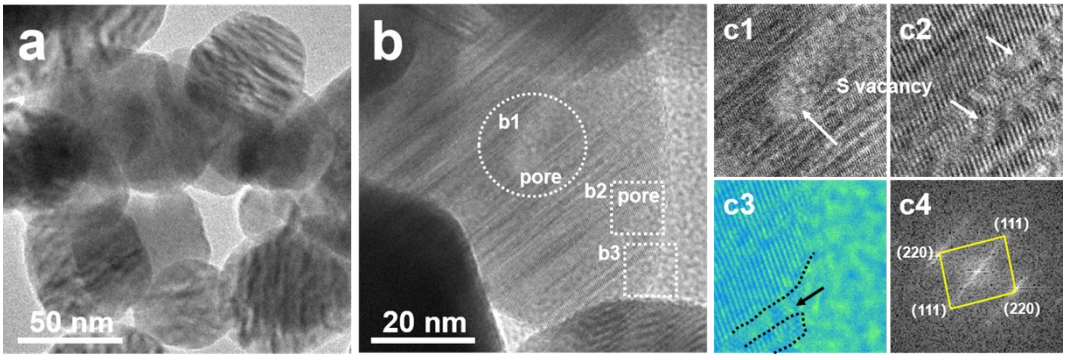

Fig. S7 (a) TEM image and (b) HRTEM image of *Sv*-ZCS sample. (c1-c3) HRTEM images of the selected areas in (b) marked with b1, b2, and b3. (c4) FFT image performed from the selected area in b2.

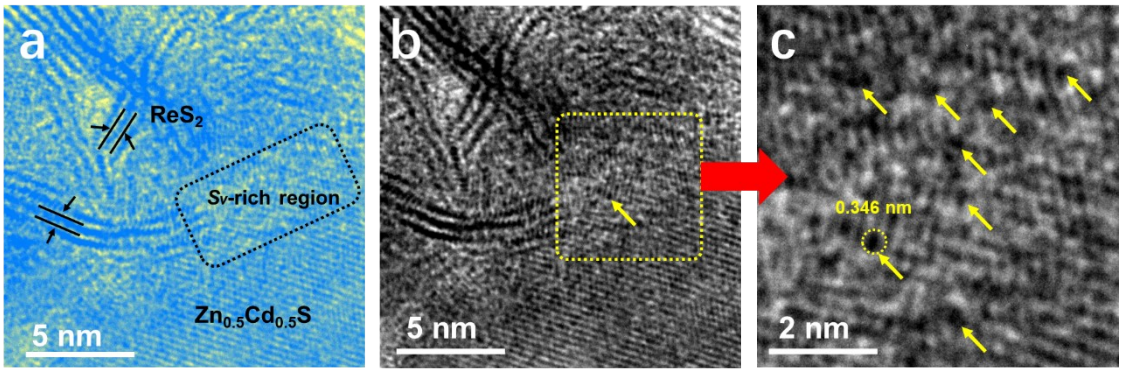

Fig. S8 (a) Pseudo Color HRETM image and (b and c) HRETM images of ReS_2/*Sv*-ZCS composite.

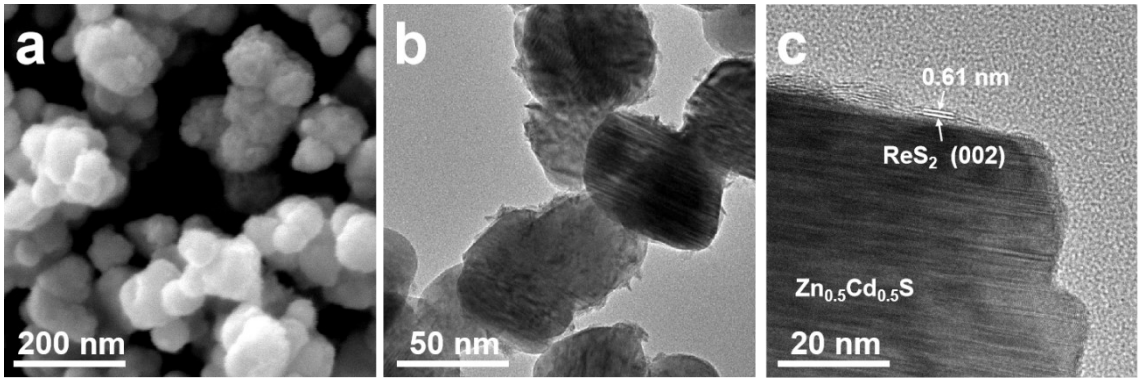

Fig. S9 (a) SEM image, (b) TEM image, (c) HRTEM image of ReS_2/ZCS sample.

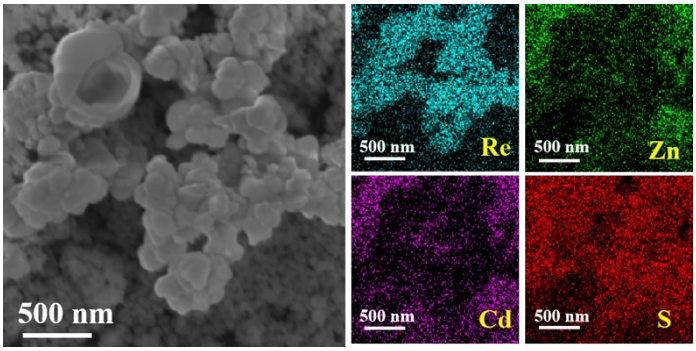

Fig. S10 Element mapping images of ReS_2/*Sv*-ZCS sample.

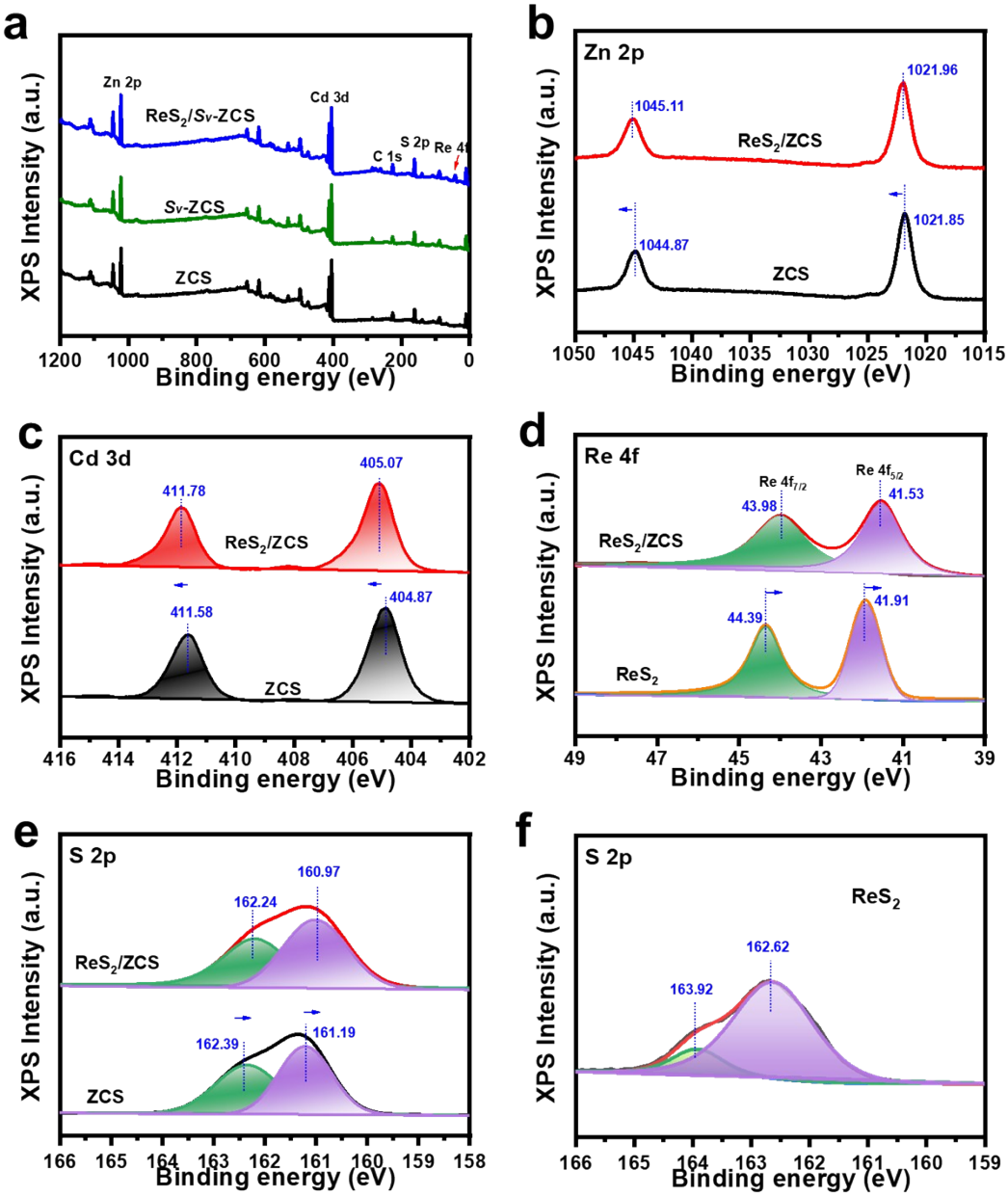

Fig. S11 (a) Survey XPS spectra of ZCS, *Sv*-ZCS, and ReS_2/*Sv*-ZCS samples. (b) Zn 2p, (c) Cd 3d, (d) Re 4f, and (e) S 2p XPS spectra of ZCS and ReS_2/ZCS samples. (f) S 2p XPS spectra of pure ReS_2.

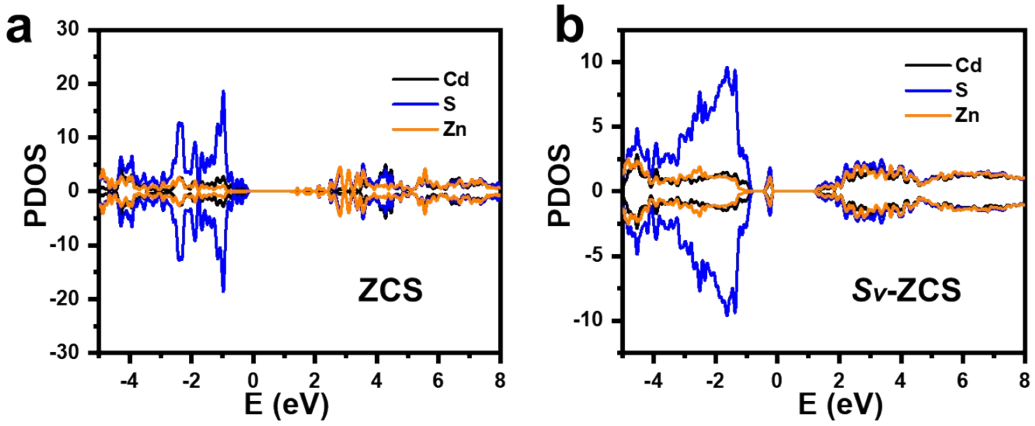

Fig. S12 Density of states (DOS) of ZCS and *Sv*-ZCS.

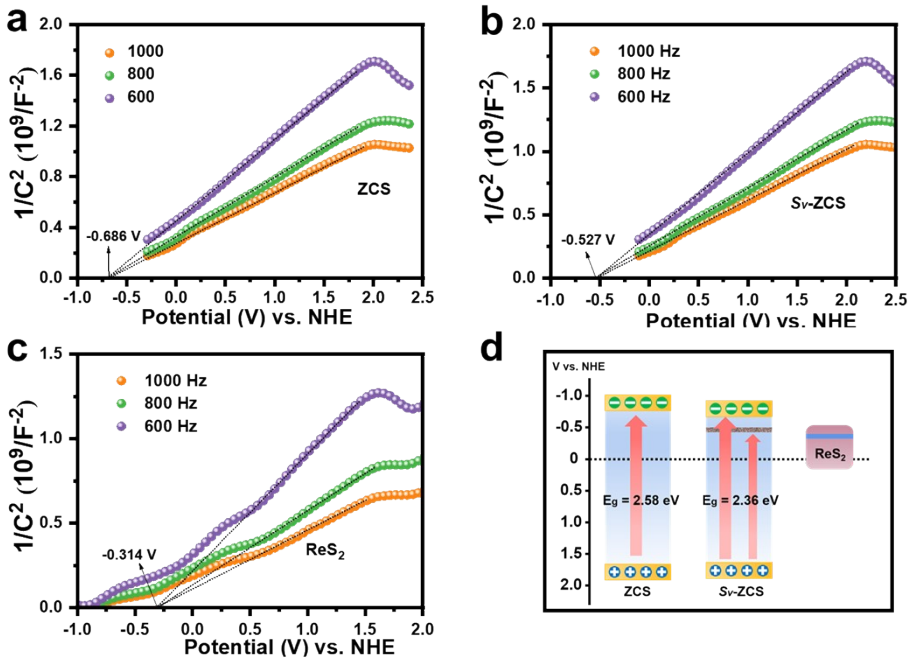

Fig. S13 Mott-Schottky plots of (a) ZCS, (b) *Sv*-ZCS and (c) ReS_2 samples. (d) Schematic diagram of band structure for as-prepared photocatalysts.

Notes 4: Mott–Schottky plots were constructed to define the types of conductivity and band potential for semiconductors. The positive slopes in Fig. S10 indicate that both ZCS and *Sv*-ZCS are n-type semiconductors. The calculated flat-band potentials of ZCS and *Sv*-ZCS were estimated to be -0.686 V and -0.527 V vs. NHE, respectively. It is known that the conduction band potential (E_{CB}) for n-type semiconductor is more negative about -0.1 or -0.2 V than its flat band potential.[11] Therefore, the E_{CB} for ZCS and *Sv*-ZCS are roughly reckon up to -0.886 V and -0.727 V vs. NHE. The band gap values of ZCS and *Sv*-ZCS are determined to be 2.58 eV and 2.36 eV via Kubelka-Munk function. Using formula $E_g = E_{VB}$-E_{CB}, the valance band (VB) potential of ZCS and *Sv*-ZCS were calculated to be +1.694 V and +1.633 V, respectively. The flat band potential of ReS_2 is determined to be -0.314 V vs. NHE from the *x*-intercepts in the corresponding M-S plot. The detailed information of band structure is displayed in Fig. S10d.

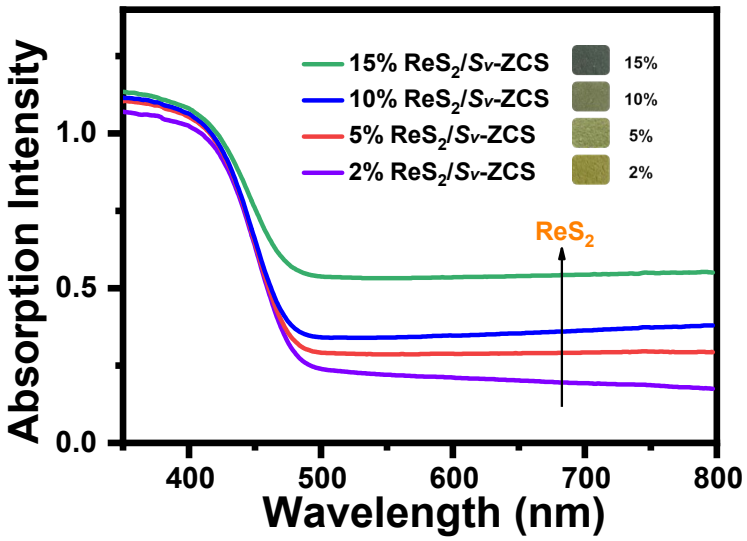

Fig. S14 UV-Vis diffuse reflectance spectra of ReS_2/*Sv*-ZCS with different content of ReS_2.

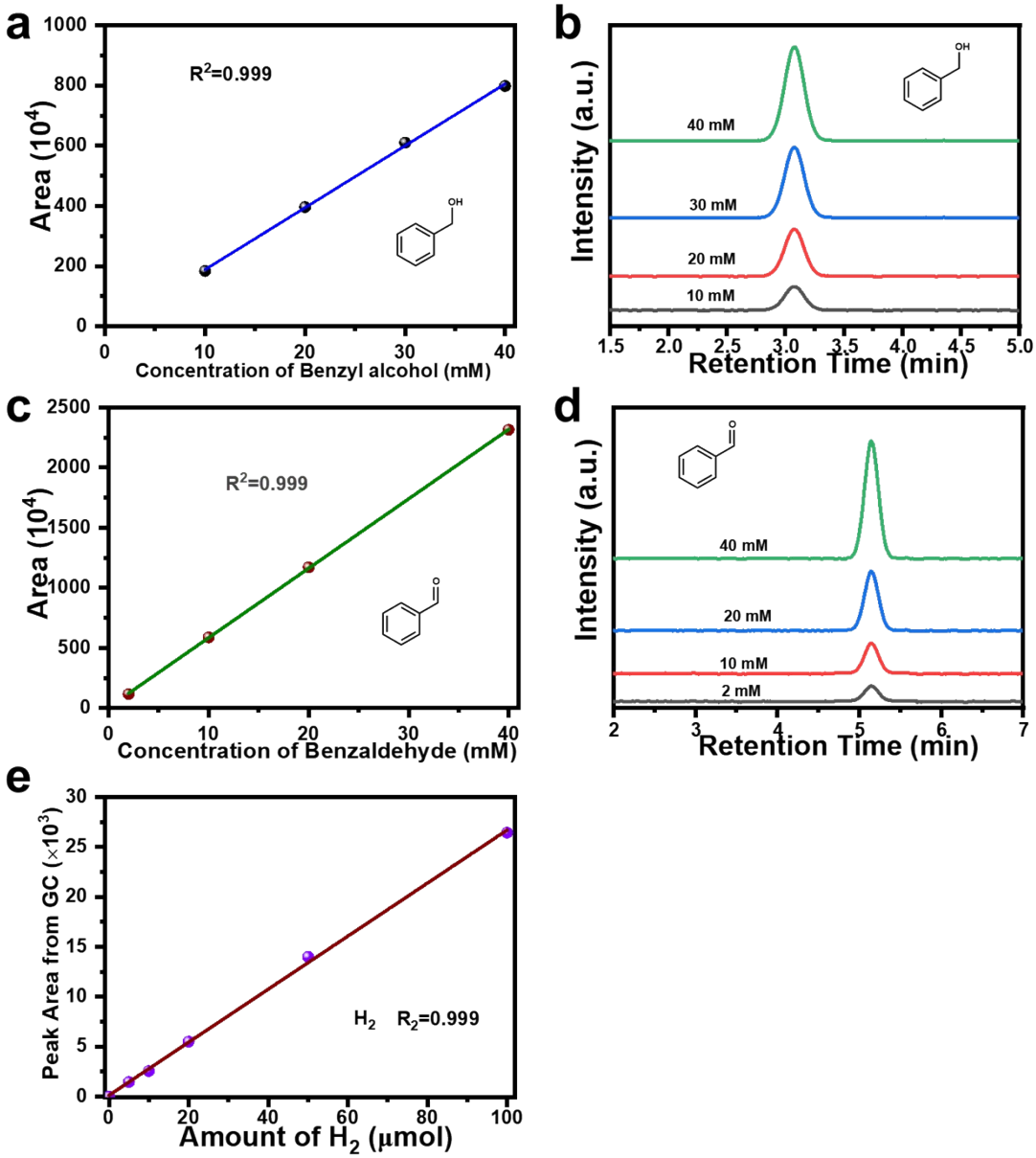

Fig. S15 The peak areas for the known product concentrations were used to generate a calibration curve of (a) benzyl alcohol, (c) benzaldehyde and (e) H_2. High performance liquid chromatography (HPLC) analysis chromatogram of (b) benzyl alcohol and (d) benzaldehyde.

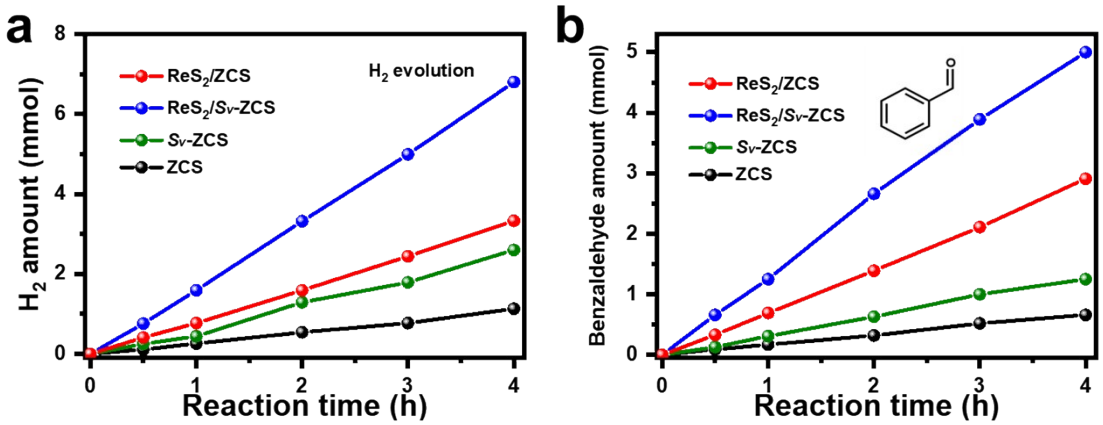

Fig. S16 (a) H_2 and (b) benzaldehyde production amount with different reaction time upon ZCS, *Sv*-ZCS, ReS_2/ZCS and ReS_2/*Sv*-ZCS samples.

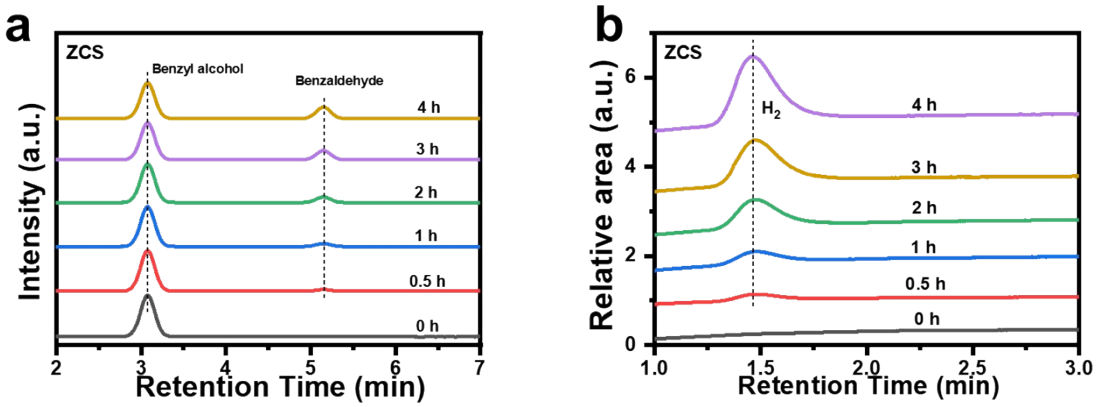

Fig. S17 (a) HPLC analysis of intermediate products and (b) GC analysis of H_2 products over ZCS sample in the photocatalytic reaction process.

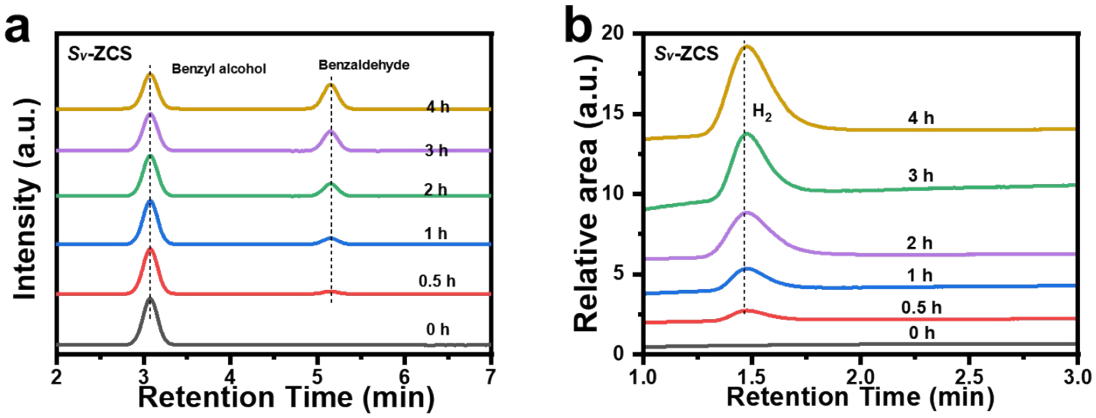

Fig. S18 (a) HPLC analysis of intermediate products and (b) GC analysis of H_2 products over *Sv*-ZCS sample in the photocatalytic reaction process.

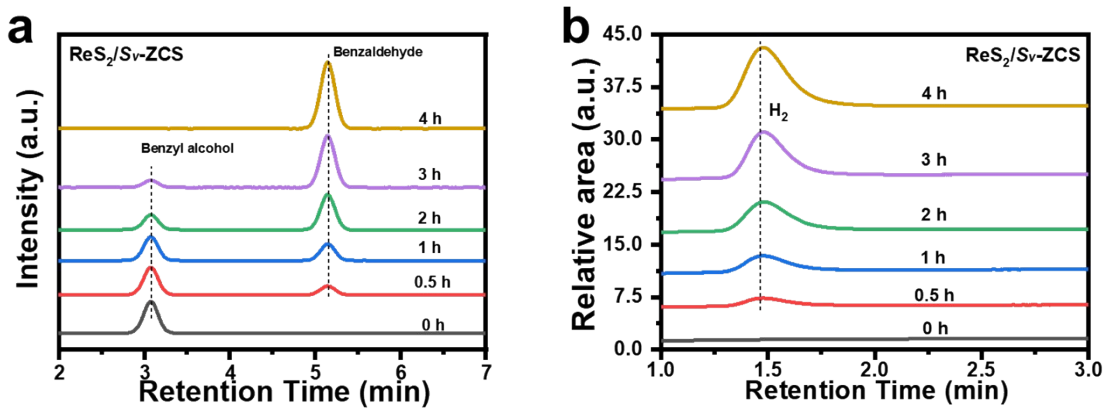

Fig. S19 (a) HPLC analysis of intermediate products and (b) GC analysis of H_2 products over ReS_2/*Sv*-ZCS sample in the photocatalytic reaction process.

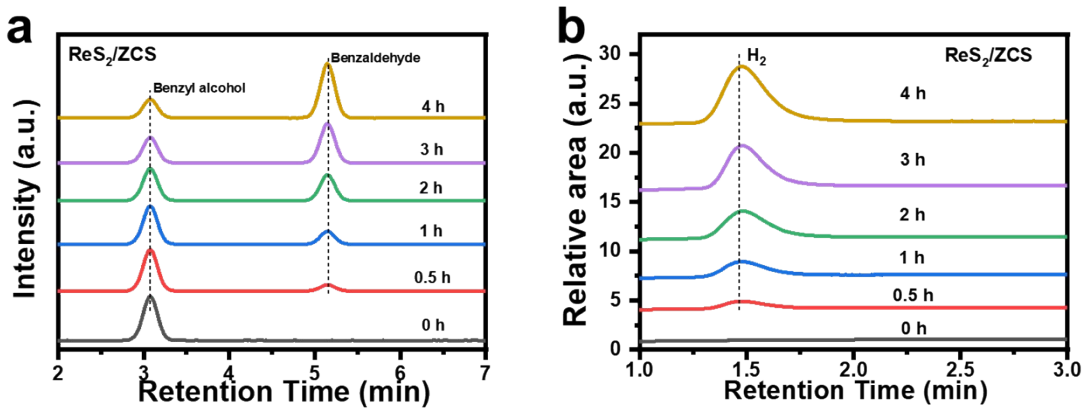

Fig. S20 (a) HPLC analysis of intermediate products and (b) GC analysis of H_2 products over ReS_2/ZCS sample in the photocatalytic reaction process.

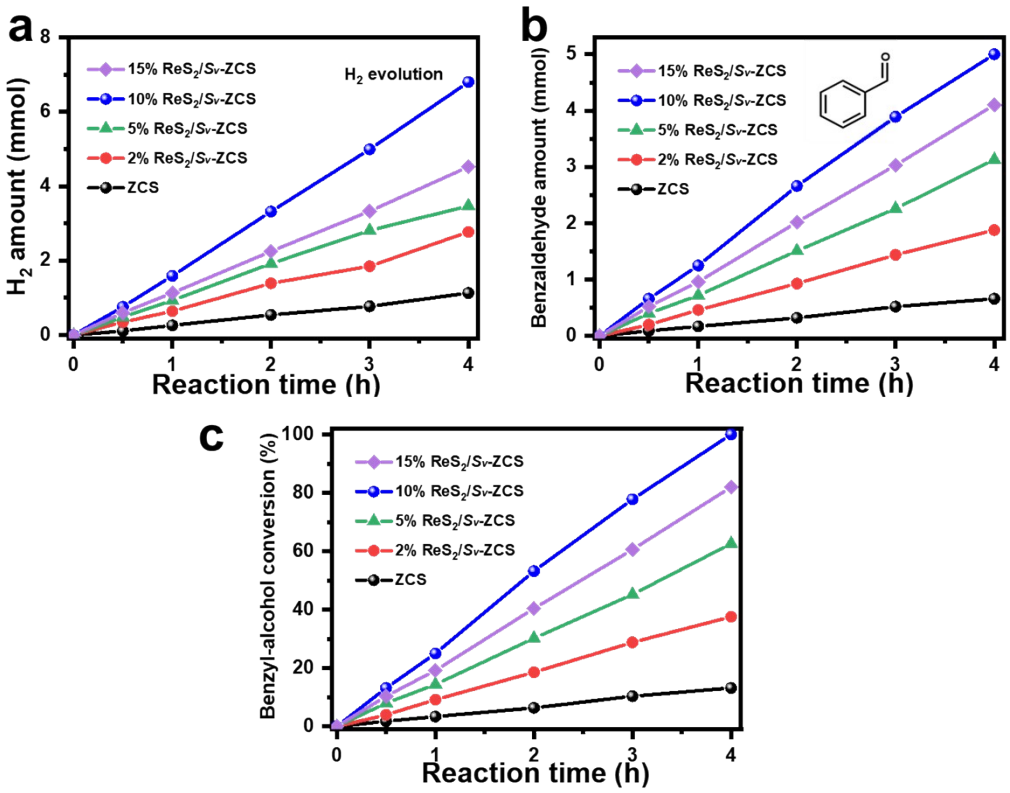

Fig. S21 Photocatalytic activity of (a) H_2 and (b) benzaldehyde production amount, (c) benzyl-alcohol conversion with different reaction time upon ZCS and ReS_2/*Sv*-ZCS samples with different amount of ReS_2.

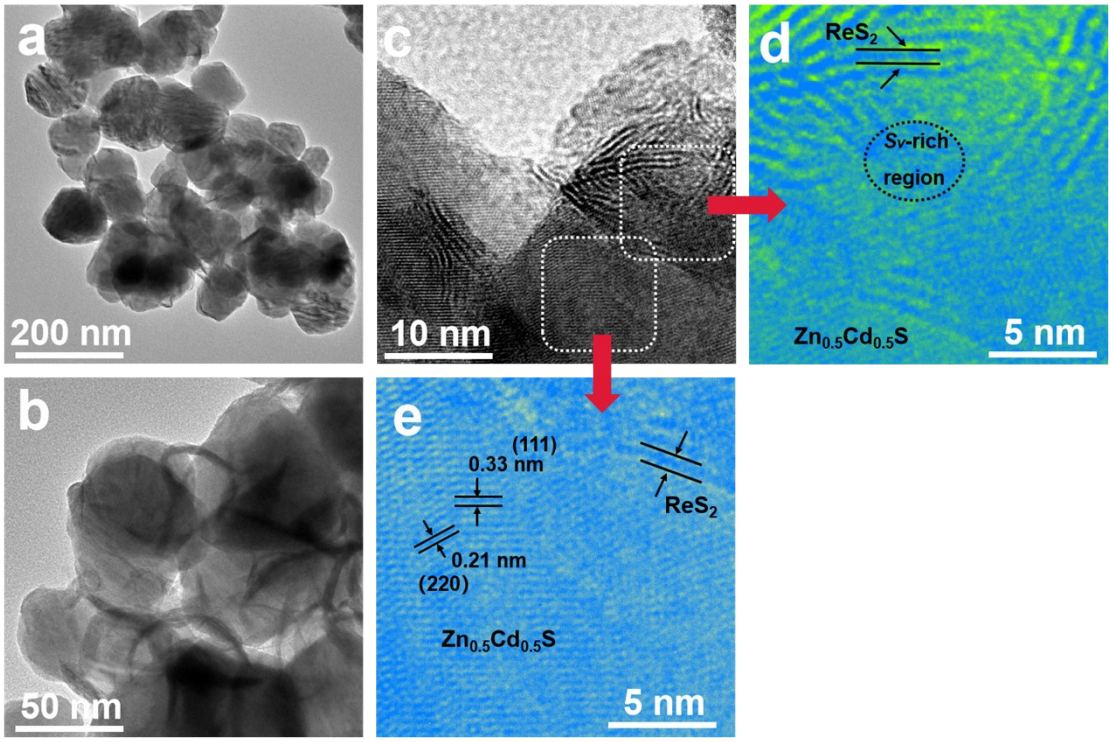

Fig. S22 (a and b) TEM and (c-e) HRTEM images of the ReS_2/*Sv*-ZCS sample after reaction.

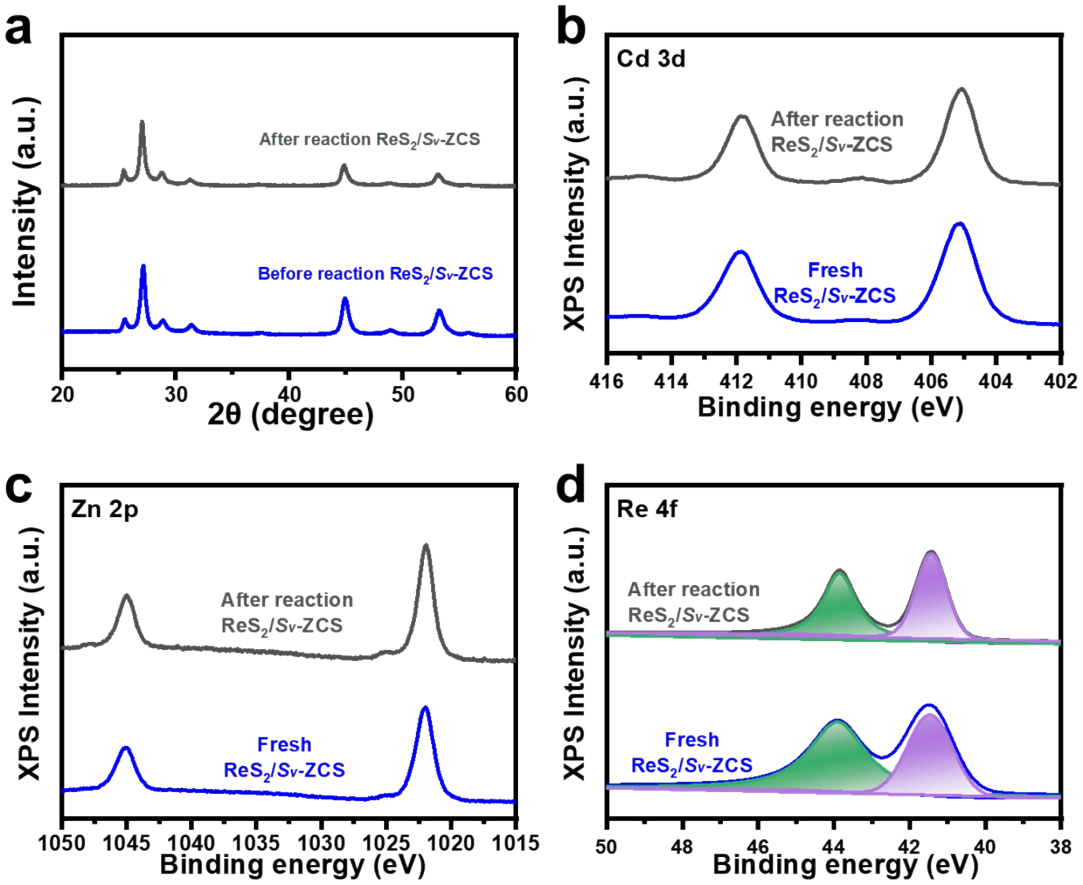

Fig. S23 (a) XRD patterns, (b) Cd 3d, (c) Zn 2p, and (d) Re 4f XPS spectra of fresh and used ReS_2/*Sv*-ZCS samples.

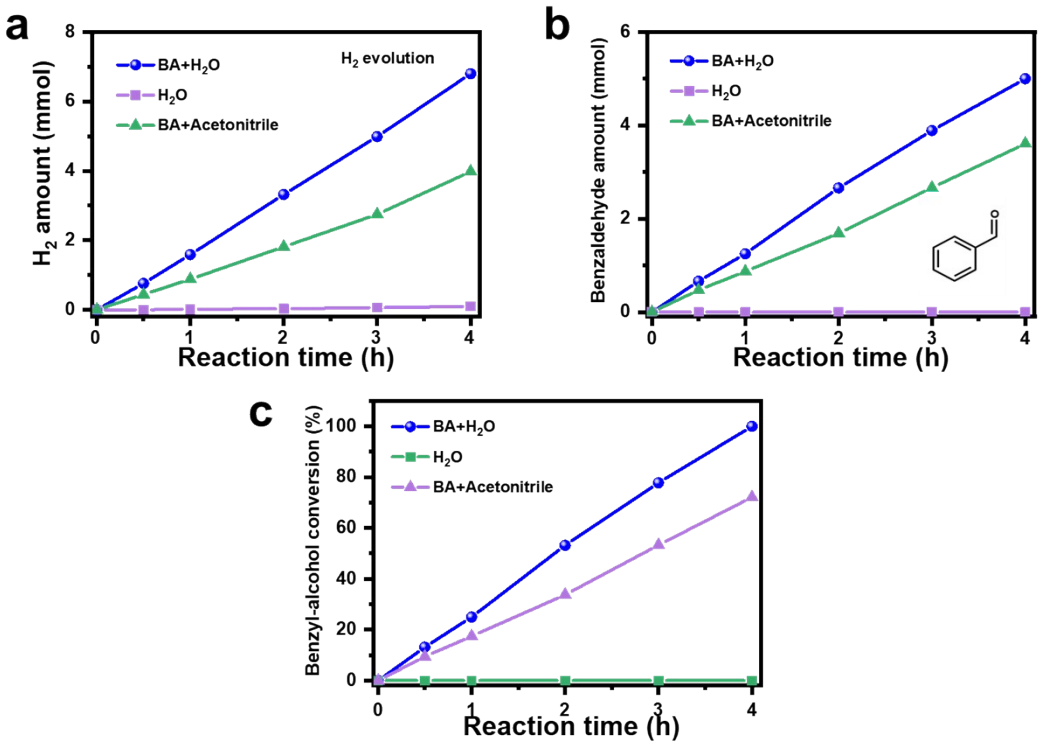

Fig. S24 Photocatalytic activity of (a) H_2 and (b) benzaldehyde evolution amount, (c) benzyl alcohol conversion with different solvent condition upon 10% ReS_2/*Sv*-ZCS sample.

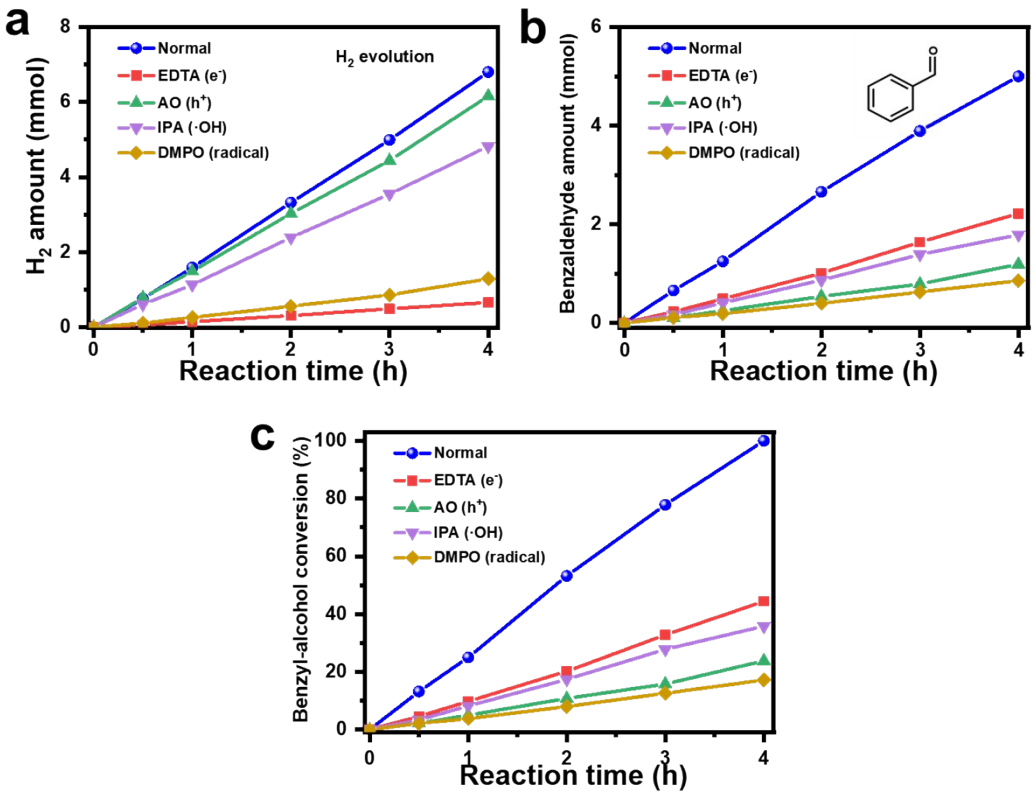

Fig. S25 Photocatalytic activity of (a) H_2 and (b) benzaldehyde evolution amount, (c) benzyl alcohol conversion with different sacrificial reagents upon 10% ReS_2/*Sv*-ZCS sample.

Table S1 Element analysis of ZCS, *Sv*-ZCS, ReS_2/*Sv*-ZCS and ReS_2/ZCS samples.

Sample	Element content (Atom%)				Atomic ratio of Zn:Cd:S by ICP analysis
	Zn	Cd	S	Re	
ZCS	24.29	23.85	51.86	/	**1.018 : 1 : 2.174**
***Sv*-HZCS**	24.12	25.53	50.35	/	**0.945 : 1 : 1.972**
***Sv*-ZCS**	23.96	25.80	50.24	/	**0.929 : 1 : 1.947**
ReS_2/*Sv*-ZCS	23.90	23.11	52.29	2.59	**1.033 : 1 : 2.465**
ReS_2/ZCS	23.45	22.78	51.59	2.18	**1.029 : 1 : 2.260**

Table S2 The experimental data of Brunauer-Emmett-Teller (BET) and Pore diameter of ZCS, *Sv*-ZCS, ReS_2/ZCS and ReS_2/*Sv*-ZCS samples.

Sample	Surface area $[m^2g^{-1}]$	Pore Volume $[cm^3/g]$	Pore Size [nm]
ZCS	13.31	0.0357	10.84
***Sv*-ZCS**	20.01	0.0576	11.51
ReS_2/ZCS	18.60	0.0577	12.40
ReS_2/*Sv*-ZCS	28.72	0.1253	14.43

Table S3. The measured conductivity (σ), carrier mobility (μ), carrier concentration (c), and I/V using electrochemical characterization.

Sample	I/V (μA/V)	σ (S·m^{-1})	c (cm^{-3})	μ (cm^2·V^{-1}·s^{-1})[1]
ZCS	0.067	0.002	2.4×10^{15}	0.031
***Sv*-ZCS**	0.51	0.016	4.2×10^{15}	0.196
ReS_2/ZCS	1.1	0.036	5.8×10^{15}	0.387
ReS_2/*Sv*-ZCS	1.85	0.061	6.1×10^{15}	0.625

[1] The carrier mobility (μ) of ZCS, *Sv*-ZCS, ReS_2/ZCS and ReS_2/*Sv*-ZCS samples is calculated according to the following equations:[12]

$$\sigma = \frac{dI}{(2n-1)LhV}$$

$$\sigma = cq\mu$$

Where d is the interelectrode spacing (75 μm), I is the current, n is the number of electrode digits (the interdigitated array electrode in our measurement is composed of n =10 pairs of ITO electrode digits deposited onto a glass substrate), L is the overlapping length of the electrodes (6000 μm), h is the film thickness (20 nm), c is the charge carrier's concentration, and q stands for elementary charge (1.6×10^{-19} C). According to the dynamic current-voltage curves in Fig. 5b, the value of I/V for ZCS, *Sv*-ZCS, ReS_2/ZCS and ReS_2/*Sv*-ZCS samples is 0.067, 0.51, 1.1, and 1.85 μA/V, respectively. Take the ReS_2/*Sv*-ZCS sample as example, the detailed calculation process for conductivity (σ) and carrier mobility (μ) is following:

$$\sigma = \frac{dI}{(2n-1)LhV} = \frac{75\times10^{-6}\text{m}}{(2\times10-1)\times6000\times10^{-6}\text{m}\times20\times10^{-9}\text{m}} \times 1.85\times10^{-6}\ A/V = 0.061\ \text{S·m}^{-1}$$

$$\mu = \frac{\sigma}{cq} = \frac{0.061\ \text{S·m}^{-1}}{6.1\times10^{15}\times10^{6}\ \text{m}^{-3}\times1.6\times10^{-19}\ \text{C}} = 6.25\times10^{-5}\text{m}^2\text{·V}^{-1}\text{·s}^{-1} = 0.625\ \text{cm}^2\text{·V}^{-1}\text{·s}^{-1}$$

Table S4 Time constant τ and the fluorescence quantum yield of photocatalysts

Sample	Absolute fluorescence quantum yield	τ_1 (ns)	%	τ_2 (ns)	%	τ_{ave} (ns)[1]
ZCS	7.26%	1.47	33.17	10.15	66.83	7.26
***Sv*-ZCS**	5.31%	2.23	15.83	14.68	84.17	13.15
ReS_2/*Sv*-ZCS	0.62%	1.29	37.16	7.20	62.84	5.05
ReS_2/ZCS	0.86%	1.34	25.34	8.11	62.62	5.58

[1.] the average lifetimes (τ_{ave}) for ZCS, ReS_2/ZCS, *Sv*-ZCS, and ReS_2/*Sv*-ZCS samples have been obtained through the kinetic decay parameters $\tau_{ave} = \frac{\sum_i A_i\tau_i}{\sum_i A_i}$. The detailed calculation process for injection rate is following:[13]

$$k_{ET}(\text{for } ReS_2/ZCS) = \frac{1}{5.58\times10^{-9}\ \text{s}} - \frac{1}{7.27\times10^{-9}\ \text{s}} = 4.15\times10^{7}\ \text{s}^{-1}$$

$$k_{ET}(\text{for } ReS_2/Sv\text{-}ZCS) = \frac{1}{5.05\times10^{-9}\ \text{s}} - \frac{1}{13.15\times10^{-9}\ \text{s}} = 1.22\times10^{8}\ \text{s}^{-1}$$

Table S5 Black experiments without catalyst nor light irradiation. [a]

Entry	Photocatalyst	Irradiation condition	Amount of H_2 evolution (mmol)	Amount of benzaldehyde evolution (mmol)
1	10% ReS_2/*Sv*-ZCS	/	/	/
2	/	> 420 nm	/	/

[a] Reaction conditions: 10 mg 10% ReS_2/*Sv*-ZCS, 0.5 mmol of benzyl alcohol, total 4-hour reaction time; gas and liquid mixtures were determined by GC and HPLC, respectively.

Table S6 Comparison for H_2 and aldehydes production with other photocatalysts in recent works.

Photocatalyst	**Solvent**	**Light source**	**Rate of H_2 evolution (mmol/g/h)**	**Rate of aldehydes (mmol/g/h)**	**Aldehydes selectivity (%)**	**Reference**
ReS_2/*Sv*-ZCS	Water	$\lambda \geq 420$ nm	159	125	>99	This work
Ni/$Zn_{0.5}Cd_{0.5}S$	/	$\lambda \geq 420$ nm	5.4	1.49	57.7	*J. Energy. Chem.* **2019,** *30,* 71
Ru/g-C_3N_4	Water	Xe lamp ($320 \leq \lambda \leq 850$)	6.42	5.07	>99	*Applied Catal. B,* **2022,** *315,* 121575
MoS_2/$ZnIn_2S_4$	Water	$\lambda \geq 420$ nm	1.38	1.42	/	*Applied Catal. B,* **2021,** *298,* 120541
CN_x-NiP	KP_i water	AM 1.5 G	15.26	14.53	>99	*J. Am. Chem. Soc.* **2016,** *138,* 9183

References

1. G. Kresse, *J. Non-Cryst. Solids*, 1995, **192-193**, 222-229.
2. G. Kresse and J. Furthmuller, *Phys. Rev. B Condens. Matter.*, 1996, **54**, 11169-11186.
3. P. E. Blochl, *Phys. Rev. B Condens. Matter.*, 1994, **50**, 17953-17979.
4. G. Kresse and D. Joubert, *Phys. Rev. B*, 1999, **59**, 1758-1775.
5. J. P. Perdew, K. Burke and M. Ernzerhof, *Phys. Rev. Lett.*, 1996, **77**, 3865-3868.
6. S. Grimme, S. Ehrlich and L. Goerigk, *J. Comput. Chem.*, 2011, **32**, 1456-1465.
7. S. Grimme, J. Antony, S. Ehrlich and H. Krieg, *J. Chem. Phys.*, 2010, **132**, 154104.
8. M. Liu, L. Wang, G. Lu, X. Yao and L. Guo, *Energy Environ. Sci.*, 2011, **4**, 1372-1378.
9. G. Yu, J. Qian, P. Zhang, B. Zhang, W. Zhang, W. Yan and G. Liu, *Nat. Commun.*, 2019, **10**, 4912.
10. G. Yu, X. Zhou, H. Zhao, W. Zhang, W. Yan and G. Liu, *Solar RRL*, 2021, **5**, 2100580.
11. H. Huang, G. Yu, X. Zhao, B. Cui, J. Yu, C. Zhao, H. Liu and X. Li, *J. Energy Chem.*, 2024, **88**, 272-281.
12. Y. Chen, M. Bouvet, T. Sizun, Y. Gao, C. Plassard, E. Lesniewska and J. Jiang, *Phys. Chem. Chem. Phys.*, 2010, **12**, 12851-12861.
13. M. Abdellah, K. Žídek, K. Zheng, P. Chábera, M. E. Messing and T. Pullerits, *J. Phys. Chem. Lett.*, 2013, **4**, 1760-1765.